THE JOURNAL OF PHYSICAL CHEMISTRY C

Article

pubs.acs.org/JPCC

Dipole-Assisted Charge Separation in Organic–Inorganic Hybrid Photovoltaic Heterojunctions: Insight from First-Principles Simulations

Zi Li, Xu Zhang, and Gang Lu*

Department of Physics and Astronomy, California State University, Northridge, California 91330, United States

ABSTRACT: It has been observed that the external quantum efficiency (EQE) of a hybrid organic/inorganic (P3HT/ZnO) solar cell can be tripled by inserting a monolayer of fullerene (PCBA) at the donor (P3HT) and acceptor (ZnO) interface. First-principles simulations are performed to understand the origin of the increased EQE, offering a complementary perspective to the experiment. The interfacial atomic and electronic structure as well as energy alignment are examined for both the bare and PCBA-modified interface. The presence of PCBA induces an interfacial dipole and shifts up the lowest-unoccupied-molecular-orbital (LUMO) level of P3HT relative to the conduction band edge of ZnO. Interfacial electron dynamics including forward and backward charge transfer time scales are estimated. We find that the two interfaces have similar forward electron transfer rates but their transfer mechanisms differ. The PCBA-modified interface exhibits a weaker adiabatic but a stronger nonadiabatic charge transfer. In contrast, the charge recombination time scale of the modified interface is 20 times slower than that of the bare interface, thanks to reduced donor/acceptor wave function coupling as well as increased donor/acceptor energy offset. By slowing down the charge recombination, the PCBA-modified heterojunction offers the superior performance observed in the experiment.

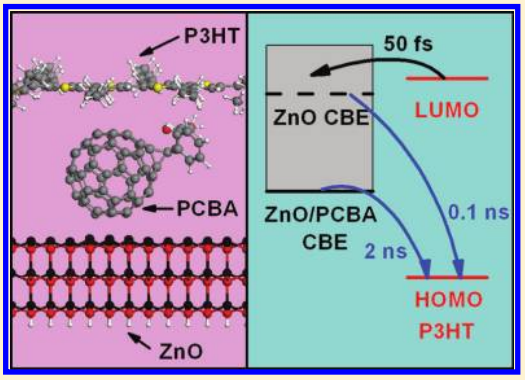

INTRODUCTION

All-organic and hybrid (organic/inorganic) photovoltaic heterojunctions[1,2] represent cost-effective and lightweight alternatives to the traditional silicon-based solar cells. Both the organic and hybrid photovoltaics rely on interfacial exciton dissociation and charge separation to produce photocurrent, and both have their respective strength and weakness. The defining difference between the all-organic and hybrid solar cells is their acceptor materials: in the organic solar cells, the acceptors are typically fullerene derivatives such as phenyl-C61-butyric acid methyl ester (PCBM), phenyl-C61-butyric acid (PCBA), and C_{60}. In contrast, the acceptors in the hybrid solar cells are inorganic semiconductors, primarily transition-metal oxides, such as ZnO and TiO_2. Compared with the fullerenes as the acceptor, the metal oxides offer higher electron mobility, superior environmental stability, and tunability of interfacial band offsets, which render the hybrid heterojunctions particularly attractive. For example, ZnO/polymer hybrid solar cells are gaining considerable interest thanks to the favorable film quality and electronic properties of ZnO.[2−7] Furthermore, one can dramatically increase the interfacial areas of the hybrid heterojunctions by exploring oxide nanostructures, in an effort to mimic the bulk heterojunctions. However, despite the aforementioned advantages, the hybrid solar cells suffer a critical drawback: they produce far lower photocurrents as compared to all-organic counterparts.[2] This drawback is so severe that the improvement of photocurrents has been regarded as the highest research priority for the hybrid solar cells.

It has been recognized that enhancing interfacial charge separation and reducing interfacial charge recombination are the most crucial factors for boosting the photocurrents. One promising strategy is to optimize the interfacial energy offset by introducing an organic layer at the oxide/polymer interface. For example, molecular interfacial modifiers (IMs) can be inserted at the donor/acceptor interface to generate an interfacial dipole and to produce a desirable interfacial energy offset for charge separation.[8−13] The fullerene derivatives have been widely used as IMs because of their tunable energy levels, decent electron mobility, and favorable compatibility to the active layer.[14−21] Herein, we focus our attention on a successful experimental demonstration of using PCBA as an IM to improve the performance of a hybrid solar cell. Specifically, we provide a theoretical perspective on a recent experiment[21] which has achieved a 3-fold increase of EQE by incorporating a self-assembled monolayer of PCBA at the donor/acceptor interface. The hybrid heterojunction consists of poly(3-hexylthiophene) (P3HT) as the donor and n-type ZnO as the acceptor along with the PCBA monolayer at the donor/acceptor interface. In contrast to a large body of experimental research, relevant theoretical effort has been scarce for the hybrid heterojunctions.

Received: December 20, 2011
Revised: April 17, 2012
Published: April 18, 2012

 © 2012 American Chemical Society dx.doi.org/10.1021/jp212286r | J. Phys. Chem. C 2012, 116, 9845–9851

There was a classical molecular dynamics (MD) simulation on the interfacial atomic structure of the ZnO/P3HT heterojunction[22] and a first-principles calculation on the interfacial electronic structure of ZnO/P3HT.[23,24] However, all of these studies concerned only the bare interface in the absence of any IM; no theoretical investigation has ever been afforded to elucidate the effect of IMs on interfacial charge separation. To this end, we perform first-principles simulations to study the atomic and electronic structure of the ZnO/P3HT interface with and without the PCBA monolayer. In particular, we determine the PCBA-induced interfacial dipole as well as the energy offset at the interface. The phonon-assisted electron dynamics is simulated to estimate interfacial charge transfer rates. Both forward and backward (or recombination) charge transfers are considered. Overall, the theoretical results are in excellent agreement with the experiment, offering insight that is not available from the experimental investigation alone.

THEORETICAL FRAMEWORK AND COMPUTATIONAL DETAILS

***Ab Initio* Non-Adiabatic Molecular Dynamics.** Two types of charge transfer are considered in the paper: a ground state charge transfer and an excited state charge transfer. As the name indicated, the former takes place in the electronic ground state while the latter involves a photoexcited electron making transitions between the donor and the acceptor states. For simplicity, we refer to the excited state charge transfer as charge transfer throughout the rest of the paper. The charge transfer is modeled by *ab initio* non-adiabatic molecular dynamics (NAMD), in which a photoexcited (PE) electron can transfer (forward) from the P3HT LUMO to the conduction bands of the acceptor, or (backward) from the ZnO conduction bands to the highest occupied molecular orbital (HOMO) of P3HT. The determination of the forward and backward electron transfer rates is one of the main objectives of the work. Specifically, the *ab initio* NAMD[25−27] combined with a modified surface-hopping formalism[28,29] is used to capture the phonon-assisted charge transfer across the donor/acceptor interface. In this method, the wave function of the PE state $\psi_{PE}(\mathbf{r}, t)$ is expanded in the basis of adiabatic Kohn−Sham (KS) orbitals determined from the static KS-DFT calculations at an ionic configuration $\{\mathbf{R}_i(t)\}$

$$\psi_{PE}(\mathbf{r}, t) = \sum_k c_k(t)\phi_k(\mathbf{r}, \mathbf{R}_i(t)) \tag{1}$$

Here, ϕ_k is the kth KS orbital at time t, $c_k(t)$ is the expansion coefficient, and the sum is over all adiabatic KS orbitals at time t. The positions of all ions at time t are labeled collectively by $\{\mathbf{R}_i(t)\}$. Substituting eq 1 into the time-dependent DFT (TDDFT) equation in which H_{KS} is the time-dependent KS Hamiltonian,

$$i\hbar\frac{\partial}{\partial t}\psi_{PE}(\mathbf{r}, t) = H_{KS}(\mathbf{r}, \mathbf{R}, t)\psi_{PE}(\mathbf{r}, t) \tag{2}$$

one obtains the time evolution of the coefficient $c_k(t)$:

$$\frac{\partial}{\partial t}c_j(t) = -\sum_k c_k(t)\left(\frac{i}{\hbar}\varepsilon_k\delta_{jk} + d_{jk}\right) \tag{3}$$

where ε_k is the energy of the adiabatic KS orbital k and d_{jk} is the nonadiabatic coupling between the KS orbitals j and k

$$d_{jk} = \langle\phi_j|\nabla_{\mathbf{R}}|\phi_k\rangle\cdot\frac{d\mathbf{R}}{dt} = \langle\phi_j|\frac{\partial}{\partial t}|\phi_k\rangle \tag{4}$$

which represents the electronic coupling between the KS orbitals owing to the ionic motion. ε_k and d_{jk} are obtained from a 1000 fs-long *ab initio* Born−Oppenheimer MD (BOMD), performed prior to the NAMD simulations. The time-domain TDDFT method has been extensively used to describe excited state charge transfer,[25−27,30−32] and its validity has been examined recently.[33]

On the basis of the coefficient $c_j(t)$, one can determine the electron transition rates following either Ehrenfest or surface-hopping dynamics. In the Ehrenfest dynamics, the PE electron can simultaneously occupy many adiabatic KS states and the probability amplitude in a particular state j at time t is given by $|c_j(t)|$. In the surface-hopping dynamics, the PE electron is assumed to stay in one adiabatic KS state at a time, but it can hop from one state to another. The hopping probability can be determined from $c_j(t)$,[28,29] and many surface-hopping trajectories have to be averaged to provide a statistical description of the electron dynamics. The surface-hopping dynamics has an important advantage over the Ehrenfest dynamics—it satisfies the detailed balance.[34] To capture the stochastic nature of the coupled electron-ion dynamics, 100 short NAMD trajectories—each corresponding to evolving eq 3 for 200 fs—are averaged to determine the electron transfer dynamics.[27]

To simulate the photoexcited electron transfer, the PE electron is initially placed in the P3HT LUMO, and the amount of the electron transfer (ET) at time t can be characterized by the fraction of the PE electron transfer from the LUMO to the acceptor states

$$\mathrm{ET}(t) = \sum_i p_i(t)\int_V |\phi_i(\mathbf{r}, \mathbf{R}(t))|^2\,d\mathbf{r} \tag{5}$$

where $p_i(t)$ is the occupation probability of the ith KS orbital, determined by Monte Carlo sampling over the surface-hopping trajectories.[28,29] The sum involves all KS orbitals, and the integration is over the volume (V) of the acceptor. Taking the time derivative of eq 5, one obtains two contributions:

$$\frac{d}{dt}\mathrm{ET}(t) = \sum_i \left\{\frac{dp_i}{dt}\int_V |\phi_i(\mathbf{r}, \mathbf{R}(t))|^2\,d\mathbf{r} + p_i\frac{d\int_V |\phi_i(\mathbf{r}, \mathbf{R}(t))|^2\,d\mathbf{r}}{dt}\right\} \tag{6}$$

The first term represents the nonadiabatic (NA) electron transfer, corresponding to the changes in the occupation of the adiabatic states; i.e., the PE electron hops from one state to another for charge transfer. The second term represents the adiabatic contribution, corresponding to the changes in the adiabatic charge densities themselves; i.e., the PE electron remains in the same KS orbitals while these orbitals are evolving. The contributions of the nonadiabatic ET, adiabatic ET, and the initial ET at $t = 0$ add up to the total ET.

Simulation Models and Parameters. The *ab initio* BOMD and static structural optimization are performed with the plane-wave pseudopotential method as implemented in the VASP code.[35,36] In this work, the PBE functional[37] is used to determine the atomic structure, while the hybrid PBE0 functional[38,39] is applied to calculate the electronic structure, including energy levels and wave functions of the interface. This

dx.doi.org/10.1021/jp212286r | J. Phys. Chem. C 2012, 116, 9845−9851

combination of accuracy and efficiency is motivated by the fact that the PBE functional has been shown to yield accurate atomic structure for both P3HT[40] and ZnO,[41] and the energy levels determined by PBE0 with the atomic structure obtained by PBE agree very well with the experimental results for the oligothiophene/ZnO interface.[24] The BOMD calculation is carried out at the Gamma point only, and the energy cutoff of the plane-wave basis is 400 eV. The initial atomic structure is fully relaxed by a static calculation, and the *ab initio* BOMD simulation is followed to ramp up the temperature to 300 K with repeated velocity scalings; the system is then kept at 300 K for 1000 fs to reach the thermal equilibrium. Finally, a microcanonical BOMD production run is performed for 1000 fs with a time-step of 1 fs. We have examined the autocorrelation function of the P3HT LUMO level during the microcanonical MD run, and found that the system is well equilibrated in 1000 fs.

The molecular structures of PCBA and P3HT as well as the interfacial structure of ZnO/PCBA/P3HT are shown in Figure 1a and b, respectively. The optimized ZnO lattice constants, *a*

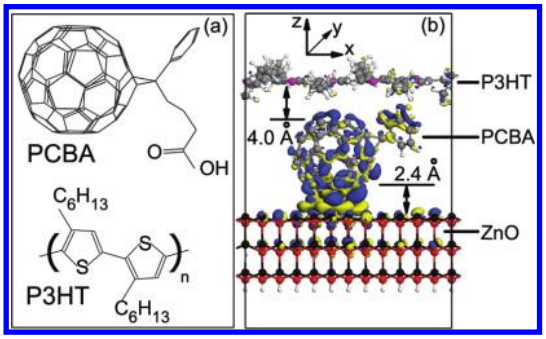

Figure 1. The atomic structure of (a) PCBA and P3HT molecules and (b) ZnO/PCBA/P3HT heterojunction. The isosurface ($\pm 0.007e/Å^3$) in part b shows the differential charge density defined as $\rho_{diff} = \rho_{total} - (\rho_{ZnO} + \rho_{PCBA} + \rho_{P3HT})$. ρ_{total} is the total charge density of the heterojunction, and ρ_{ZnO}, ρ_{PCBA}, and ρ_{P3HT} represent the charge density of the individual units by themselves. The blue (yellow) color indicates charge accumulation (depletion) when the individual units are brought together to form the heterojunction. The ground state charge transfer from the ZnO surface to PCBA is clearly visible.

and *c*, are 3.28 and 5.31 Å, respectively, similar to the corresponding experimental values (a = 3.25 Å and c = 5.20 Å).[42] The Zn-terminated ZnO (0001) surface is selected in the study because: (1) (0001) is one of the stable surfaces observed in experiments[42,43] and (2) the unsaturated and Zn-terminated (0001) surfaces have excess electrons resembling the n-type semiconductor used in the experiment.[21] As shown later, the formation of the interfacial dipole stems from the ground state charge transfer from the ZnO surface to PCBA; thus, the n-type surface is important to the dipole formation and the enhanced charge separation observed in the experiment. The ZnO surface is modeled with a six-atomic-layer slab where the dangling bonds at the bottom oxygen layer are tied-up by hydrogen atoms. The bottom two layers of the slab including the saturating H atoms are fixed in the MD simulations to mimic the bulk environment. In the direction perpendicular to the surface, large vacuum layers are used, leading to a lattice constant of 22 Å for ZnO/P3HT and 30 Å for ZnO/PCBA/P3HT. The periodical boundary conditions are also used in the two other directions, with lattice constants of 19.7 Å in the *x* direction and 17.1 Å in the *y* direction. The length of a single thiophene ring in P3HT is calculated as 3.92 Å, in good agreement with the experimental value of 3.9 Å.[44] Because the energy gap of an infinite P3HT chain differs significantly from that of a P3HT segment or oligothiophene,[45] we impose a periodical boundary condition along the chain direction to simulate an infinite polymer chain. To this end, we include five thiophene rings along the *x* direction, yielding a tensile strain of 0.5% in order to match the lattice constant of ZnO. Fortunately, this small strain has a negligible effect on P3HT energy levels—the HOMO−LUMO gap changes merely 0.04 eV.

RESULTS AND DISCUSSION

Upon the structural relaxation, the vertical distance between the P3HT chain and ZnO surface is 3.9 Å for the bare interface; in the modified interface, the vertical distance between PCBA and ZnO (P3HT) is 2.4 Å (4.0 Å), as labeled in Figure 1b. In both interfaces, some thiophene rings are warped in the vertical direction with averaged distortions of 0.20 and 0.15 Å, respectively. Two Zn atoms are attracted to PCBA and have a vertical relaxation of 0.22 Å, out of the surface plane. The ground state charge transfer from the ZnO surface to the PCBA layer is clearly visible in Figure 1b, owing to the excess electrons at the ZnO surface and the high electron affinity of PCBA.

On the basis of the interfacial atomic structure obtained with the PBE functional, we carry out electronic structure calculations using the PBE0 functional to determine the KS energy levels; the resultant energy alignment is shown in Figure 2. For the bare interface, the HOMO−LUMO gap for ZnO and

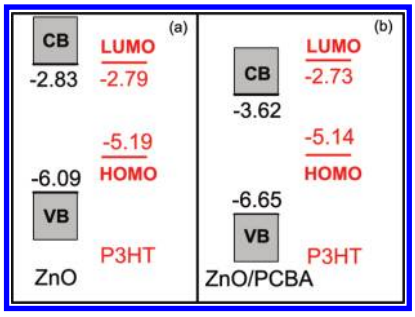

Figure 2. The schematic energy alignment of (a) the ZnO/P3HT interface and (b) the ZnO/PCBA/P3HT interface based on the PBE0 functional. The energy of the conduction band (CB) edge and the valence band (VB) edge of ZnO (black) as well as the HOMO and LUMO levels (red) of P3HT are labeled.

P3HT is 3.26 and 2.40 eV, respectively. The surface states of ZnO are removed in determining the band gap. These values are in good agreement with the experimental results of 3.4 eV for ZnO[42] and 2.0 eV for P3HT.[46] For the modified interface, we find that the band gap of P3HT is essentially unchanged, while the gap of the acceptor (ZnO/PCBA) reduces to 3.03 eV due to the ground state charge transfer from ZnO to PCBA. Comparing the two heterojunctions, we note that the energy difference between the P3HT LUMO and the ZnO conduction band edge increases significantly from 0.04 to 0.89 eV (0.85 eV increase) when the PCBA monolayer is introduced. A similar trend is also observed in the experiment where the energy difference between the P3HT LUMO and the *Fermi energy* of ZnO increases from 1.1 to 1.5 eV (0.4 eV increase).[21] The increase of the P3HT LUMO level relative to the acceptor ZnO/PCBA conduction band edge suggests that PCBA

dx.doi.org/10.1021/jp212286r | J. Phys. Chem. C 2012, 116, 9845−9851

increases the energetic driving force for the interfacial charge separation. At the same time, the PCBA LUMO (−3.70 eV) is lower than the ZnO conduction band edge. Therefore, the heterojunction does not possess the so-called "cascading band structure"—where the LUMO of an IM straddles between the LUMOs of the donor and the acceptor—as generally assumed for this type of modified heterojunctions.[47,48]

The changes in the energy offset are attributed to the interfacial dipole developed as a consequence of the ground state charge transfer from ZnO to PCBA. The interfacial dipole can be computed as

$$\mathbf{D} = \sum_i Z_i \mathbf{R}_i - \int \mathbf{r}\rho(\mathbf{r})\, d\mathbf{r} \tag{7}$$

where Z_i and $\mathbf{R}_i$ are the (positive) charge and position of the ith ion, while $\rho(\mathbf{r})$ is the electron density at $\mathbf{r}$. The dipoles along the z direction for the bare and modified interfaces are 3.8 and 7.4 eÅ, respectively, with an induced interfacial dipole of 3.6 eÅ. The ∼100% increase of the interfacial dipole could significantly change the interfacial energetic landscape. By approximating the induced dipole as a parallel-plate capacitor, one can estimate the potential energy drop across the capacitor as $\Delta E = \mathbf{D}/\varepsilon_0 S$ (S is the surface area of the plate). Using $\mathbf{D}$ = 3.6 eÅ and $S = \pi r^2$ as the cross-section area of the PCBA monolayer (r = 4.2 Å is the radius sum of PCBA and C atom), we arrive at ΔE = 0.94 eV, close to the energy increase of 0.85 eV quoted above. Therefore, the induced interfacial dipole can indeed give rise to the observed large energy shift. It should also be pointed out that the LUMO−LUMO gap between P3HT and PCBA is 0.96 eV, similar to the previously calculated LUMO−LUMO gap of 0.82 eV in the P3HT/PCBM heterojunction (PCBM is structurally very close to PCBA).[32] This similarity suggests that the dipole exists only between ZnO and PCBA, and thus, the energy offset between P3HT and PCBA is unchanged. Finally, we stress that the dipole-assisted charge separation depends on the excess electrons at the oxide surface so that the ground state charge transfer can take place, inducing the interfacial dipole. We have also examined the $(10\bar{1}0)$ ZnO surface, which undergoes a surface reconstruction eliminating the dangling bonds.[41] As a result, there is no excess electron transferred to PCBA and there is no induced dipole nor change to the energy offset.

Next, we define spatial overlap S_{ij} between two wave functions ψ_i and ψ_i as[49]

$$S_{ij} = \int d^3\mathbf{r} |\psi_i(\mathbf{r})||\psi_j(\mathbf{r})| \tag{8}$$

The overlap integrals for several pairs of wave functions are listed in Table 1 using both PBE and PBE0 functionals. We find the following: (1) the spatial overlaps between the P3HT frontier orbitals and ZnO conduction bands in the bare interface are much larger than those in the modified interface. Thus, the presence of PCBA reduces the wave function coupling between the donor and acceptor. (2) There is a significant spatial overlap between ZnO and PCBA, suggesting PCBA as an excellent interfacial modifier. (3) The overlap determined by the two functionals agrees well in general, indicating that the PBE functional can provide a reasonable description of the KS orbitals. As discussed later, the charge transfer dynamics depends crucially on the relevant wave function overlap.

In the following, we examine how the presence of the PCBA layer affects the ionic and electronic dynamics. In Figure 3, we display the partial density of states (DOS) of the ZnO conduction bands, all PCBA states, and the P3HT LUMO level, respectively, averaged over BOMD time-steps. For the bare interface, the P3HT LUMO level fluctuates above the ZnO conduction band edge, but it shifts deep inside the ZnO conduction bands in the modified heterojunction. During the ionic dynamics, the P3HT LUMO level in the bare heterojunction has a wider distribution than that of the modified interface; the standard deviation of DOS is 0.16 and 0.09 eV for the bare and the modified interfaces, respectively. The wider LUMO distribution in the bare interface can be attributed to the greater spatial coupling between the ZnO conduction bands and P3HT LUMO, as shown in Table 1. Note that, in the modified interface, the DOS of the P3HT LUMO overlaps not only with the ZnO conduction bands but

Table 1. The Orbital Overlap in the Bare and PCBA-Modified Interfaces, as Defined in eq 8 Based on the PBE0 and PBE Functionals[a]

	ψ_i	ψ_j	S_{ij} (PBE0)	S_{ij} (PBE)
bare interface	ψ_{LUMO}	ψ_{CB}	0.41	0.34
	ψ_{HOMO}	ψ_{CBE}	0.39	0.49
modified interface	ψ_{LUMO}	ψ_{CB}	0.04	0.05
	ψ_{LUMO}	$\psi^{\mathrm{PCBA}}_{\mathrm{unocc}}$	0.07	0.07
	ψ_{HOMO}	ψ_{CBE}	0.01	0.02
	ψ_{HOMO}	$\psi^{\mathrm{PCBA}}_{\mathrm{LUMO}}$	0.04	0.04
	$\psi^{\mathrm{PCBA}}_{\mathrm{LUMO}}$	ψ_{CBE}	0.43	0.34

[a]The orbitals ψ_i and ψ_j belong to P3HT and ZnO, respectively, except for the ones with superscript "PCBA". The ZnO conduction band (CB) and the unoccupied (unocc) PCBA state in ψ_j refer to the corresponding state that is the closest in energy to the P3HT LUMO. The subscript "CBE" denotes the ZnO conduction band edge.

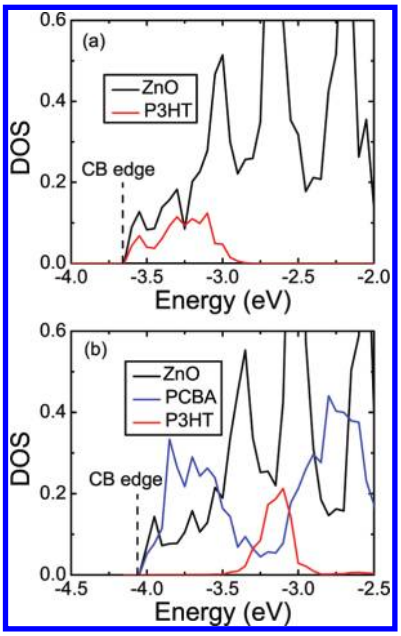

Figure 3. The density of states (DOS) of (a) the bare interface and (b) the PCBA-modified interface, averaged over BOMD configurations. The black, red, and blue curves correspond to the partial DOS of the ZnO conduction bands, all PCBA states, and the P3HT LUMO, respectively. The DOS of ZnO is downscaled by a factor of 3 so that it can be displayed clearly. The conduction band (CB) edge of ZnO is labeled by a dashed line.

dx.doi.org/10.1021/jp212286r | J. Phys. Chem. C 2012, 116, 9845−9851

also with the PCBA states, resulting in electron transfer from the P3HT LUMO to both ZnO and PCBA.

To understand the effect of lattice vibrations on charge transfer, we have calculated the Fourier transform (FT) of the P3HT LUMO shown in Figure 4. For both heterojunctions, the main FT peaks are located at the low-frequency end (less than 500 cm^{-1}), consisting of bending and torsion modes of the P3HT backbone. Thus, these phonon modes play an important role in the charge transfer. The peaks of the bare interface are much higher than those of the modified interface, indicating a larger energy fluctuation of the P3HT LUMO level, again due to the strong hybridization between the P3HT LUMO and ZnO conduction bands. Similarly, we find that the phonon modes of ZnO with frequencies less than 600 cm^{-1} [50] are also important to the charge transfer.

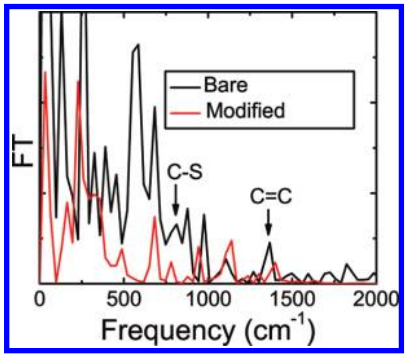

Figure 4. The Fourier transform of the P3HT LUMO energy of the bare (black) and the PCBA-modified (red) interfaces during the microcanonical BOMD simulation.

The proceeding discussion concerns the (thermodynamic) driving force for the charge separation, but it does not provide information on the kinetics or dynamics of the charge transfer. To address the latter, we conduct NAMD simulations to study electron transfer (ET) dynamics across the interface. The interfacial ET can be characterized by time-dependent electron transfer, as shown in Figure 5. The total amount of electron transfer, ET(t), is fitted to the following equation:[25]

$$\mathrm{ET}(t) = \mathrm{ET_f}\cdot\{1 - \exp[-(t + t_0)/\tau]\} \quad (9)$$

where ET(t) is obtained from the NAMD simulation at time t. From the fit, one can estimate the elapsed electron transfer time (τ) and the final amount of electron transfer (ET_f). Here, t_0 (the intercept of the time axis) is the elapsed time corresponding to the pretransferred amount. The fitted τ and ET_f are 46 fs and 0.79 for the bare interface and 47 fs and 0.84 for the modified interface. Therefore, as far as the forward charge transfer is concerned, the two heterojunctions have similar ET rates as well as the final charge transfer amount. Comparing to ZnO, there is much less charge transfer (0.07 e) onto PCBA, suggesting that PCBA does not block the electron transfer from P3HT to ZnO. Despite the reduced wave function overlap between P3HT and ZnO, the modified interface yields the similar ET time scale and charge amount as compared to the bare interface. This is because in the modified interface the P3HT LUMO lies deep inside the ZnO conduction bands and thus the charge can be transferred to many conduction bands simultaneously. On the contrary, the number of conduction bands with energies close to the P3HT LUMO level is much fewer in the bare interface.

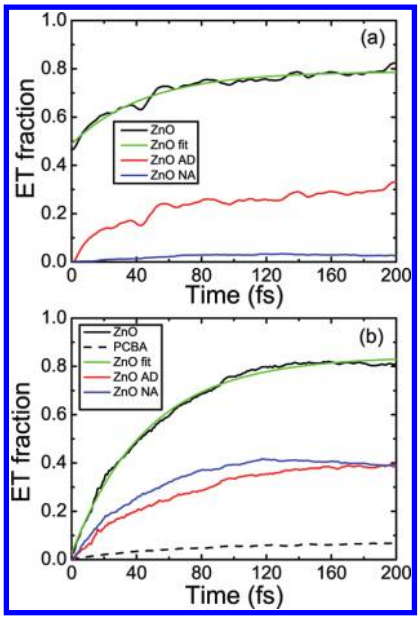

Figure 5. Electron transfer (ET) fraction from the P3HT LUMO to the ZnO conduction bands as a function of time for (a) the bare interface and (b) the PCBA-modified interface. The black, red, and blue curves correspond to the total, adiabatic (AD), and nonadiabatic (NA) transfer. The green curves are the exponential fit to the total electron transfer. In part b, the dashed curve shows the total ET to the PCBA layer.

The interfacial charge transfer can be either adiabatic or nonadiabatic. The adiabatic ET occurs when the overlap between the donor and acceptor states is significant; the nonadiabatic ET takes place when the acceptor DOS is high.[25] As shown in Figure 5a, for the bare interface, the adiabatic ET dominates owing to the larger overlap between P3HT and ZnO wave functions. On the other hand, the nonadiabatic ET is negligible because of the low DOS at the conduction band edge. For the modified interface shown in Figure 5b, the nonadiabatic ET contribution is significant owing to the high DOS of the conduction bands. The nonadiabatic ET in the modified interface makes up for the small adiabatic ET contribution and yields a similar total ET as the bare interface.

It was pointed out that the culprit behind the low internal quantum efficiency (IQE) for the bare heterojunction was back-recombination. And the high IQE of the SAM-modified devices suggests that this problem can be mitigated by the SAM deposition.[21] To shed light onto this process, we carry out simulations for the charge recombination, i.e., the charge transfer from the ZnO conduction bands to the P3HT HOMO. The time-dependent PE electron transfer is shown in Figure 6. Averaging over three initial ZnO conduction bands, we find that the final ET within 200 fs is approximately 2×10^{-3} and 9×10^{-5}, corresponding to a recombination time scale of 0.1 and 2 ns for the bare and modified interface, respectively. Therefore, the presence of PCBA can dramatically slow down the charge recombination by a factor of 20. There are two reasons for the slowed charge recombination: (1) The P3HT LUMO is the key intermediate state through which the charge recombination takes place. The charge transfer from the conduction bands to this intermediate state is significantly reduced thanks to the upshift of the LUMO relative to the conduction bands in the modified interface (cf. Figure 2). (2) The wave function overlap between ZnO and P3HT is much

dx.doi.org/10.1021/jp212286r | J. Phys. Chem. C 2012, 116, 9845−9851

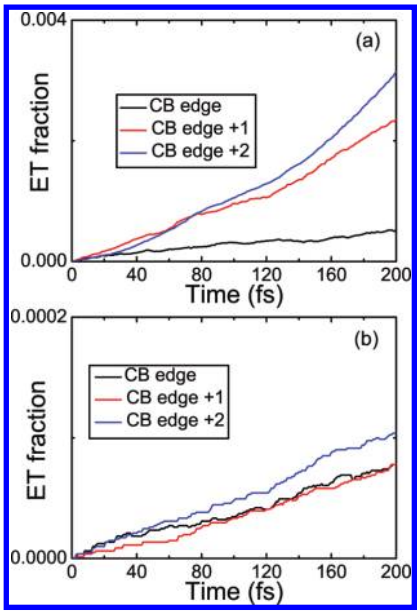

Figure 6. Electron transfer as a function of time during the recombination process in (a) the bare interface and (b) the PCBA-modified interface, respectively. The different curves correspond to the different initial states from which the electron originally resides.

smaller in the modified interface, as shown in Table 1. In the previous study of charge transfer at the P3HT/PCBM interface,[32] we found that the time scale of the charge recombination was ∼1 ns, which is similar to that of the PCBA-modified interface. This suggests that the charge transfer from PCBA (or PCBM) to P3HT is the charge recombination bottleneck, since the charge transfer from the oxides to P3HT is much faster. Experimentally, it was observed that both short-circuit current and open-circuit voltage are increased as a result of reduced recombination, in line with the simulation result. Once the charge transfer completes, the carriers will move away from the interface with a driving force provided by the energy offset between the P3HT LUMO and the conduction band edge of the acceptor. Since the energy offset is much greater in the modified interface, so is the driving force for the charge separation.

The simulations can provide some general insight for the hybrid solar cells. As discussed above, the *induced* interfacial dipole is the key for the enhanced charge separation. Since the dipole exists only between ZnO and PCBA and it is irrespective of the donor, one expects that the same mechanism should apply to other donor materials, as observed experimentally.[17] On the other hand, PCBA can lead to significant ground state charge transfer because of its high electron affinity, inducing a much larger interfacial dipole (3.6 *e*Å) than that in smaller organic IMs.[13] Furthermore, the induced dipole is perpendicular to the interface, in contrast to the intrinsic dipoles of the smaller organic IMs, which are oriented more randomly. In general, the fullerene derivatives possess a larger DOS than that of the smaller IMs, and thus have more available states to accommodate the charge transfer from the donor. Therefore, fullerenes in general and PCBA in particular are excellent candidates for IMs, consistent with the experimental findings.[20]

SUMMARY

To summarize, first-principles simulations are carried out to examine the dipole-assisted charge separation in the PCBA-modified P3HT/ZnO photovoltaic heterojunction. The atomic structure, electronic structure, and energy alignment at the interface have been studied for both the bare and modified heterojunctions. The presence of PCBA induces an interfacial dipole due to the ground state charge transfer from the ZnO surface to the PCBA monolayer, and elevates the energy position of the P3HT LUMO level relative to the ZnO conduction band edge. The electron dynamics is also studied, including both forward and backward electron transfer in order to estimate the corresponding charge transfer time scales across the interface. We find that the two heterojunctions have a similar forward electron transfer time scale but different forward transfer mechanisms. The modified interface exhibits a weaker adiabatic but a stronger nonadiabatic electron transfer compared to the bare interface. In contrast, the recombination time scale of the modified interface is 20 times slower than that of the bare interface owing to the reduced wave function coupling and the enlarged energy offset in the modified heterojunction. It is by slowing down the charge recombination that the PCBA-modified heterojunction offers the superior performance as observed experimentally.

AUTHOR INFORMATION

Corresponding Author

*E-mail: ganglu@csun.edu.

Notes

The authors declare no competing financial interest.

ACKNOWLEDGMENTS

This work was supported by NSF Solar energy grant (DMR-1035480) and the Army High Performance Computing Research Center. We acknowledge discussions with Thuc-Quyen Nguyen, Carlos Garcia-Cervera, and Gui Bazan.

REFERENCES

(1) Brabec, C. J.; Durrant, J. R. *MRS Bull.* **2008**, *33*, 670−675.
(2) Hsu, J. W. P.; Lloyd, M. T. *MRS Bull.* **2010**, *35*, 422−428.
(3) Beek, W. J. E.; Wienk, M. M.; Kemerink, M.; Yang, X. N.; Janssen, R. A. J. *J. Phys. Chem. B* **2005**, *109*, 9505−9516.
(4) Beek, W. J. E.; Wienk, M. M.; Janssen, R. A. J. *Adv. Funct. Mater.* **2006**, *16*, 1112−1116.
(5) Olson, D. C.; Piris, J.; Collins, R. T.; Shaheen, S. E.; Ginley, D. S. *Thin Solid Films* **2006**, *496*, 26−29.
(6) Koster, L. J. A.; van Strien, W. J.; Beek, W. J. E.; Blom, P. W. M. *Adv. Funct. Mater.* **2007**, *17*, 1297−1302.
(7) Greene, L. E.; Law, M.; Yuhas, B. D.; Yang, P. D. *J. Phys. Chem. C* **2007**, *111*, 18451−18456.
(8) Moser, J.; Punchihewa, S.; Infelta, P. P.; Gratzel, M. *Langmuir* **1991**, *7*, 3012−3018.
(9) Cohen, R.; Kronik, L.; Shanzer, A.; Cahen, D.; Liu, A.; Rosenwaks, Y.; Lorenz, J. K.; Ellis, A. B. *J. Am. Chem. Soc.* **1999**, *121*, 10545−10553.
(10) Kruger, J.; Bach, U.; Gratzel, M. *Adv. Mater.* **2000**, *12*, 447−451.
(11) Durrant, J. R.; Haque, S. A.; Palomares, E. *Coord. Chem. Rev.* **2004**, *248*, 1247−1257.
(12) Liu, Y. X.; Scully, S. R.; McGehee, M. D.; Liu, J. S.; Luscombe, C. K.; Frechet, J. M. J.; Shaheen, S. E.; Ginley, D. S. *J. Phys. Chem. B* **2006**, *110*, 3257−3261.
(13) Goh, C.; Scully, S. R.; McGehee, M. D. *J. Appl. Phys.* **2007**, *101*, 114503.
(14) Li, C.-Z.; Yip, H. L.; Jen, A. K. Y. *J. Mater. Chem.* **2012**, *22*, 4161−4177.
(15) Hau, S. K.; Yip, H. L.; Acton, O.; Baek, N. S.; Ma, H.; Jen, A. K. Y. *J. Mater. Chem.* **2008**, *18*, 5113−5119.

(16) Huang, J. S.; Chou, C. Y.; Lin, C. F. *Sol. Energy Mater. Sol. Cells* **2010**, *94*, 182−186.
(17) Hsieh, C. H.; Cheng, Y. J.; Li, P. J.; Chen, C. H.; Dubosc, M.; Liang, R. M.; Hsu, C. S. *J. Am. Chem. Soc.* **2011**, *132*, 4887−4893.
(18) Cheng, Y. J.; Hsieh, C. H.; He, Y. J.; Hsu, C. S.; Li, Y. F. *J. Am. Chem. Soc.* **2010**, *132*, 17381−17383.
(19) Chen, C. T.; Hsu, F. C.; Kuan, S. W.; Chen, Y. F. *Sol. Energy Mater. Sol. Cells* **2011**, *95*, 740−744.
(20) Weickert, J.; Auras, F.; Bein, T.; Schmidt-Mende, L. *J. Phys. Chem. C* **2011**, *115*, 15081−15088.
(21) Vaynzof, Y.; Kabra, D.; Zhao, L. H.; Ho, P. K. H.; Wee, A. T. S.; Friend, R. H. *Appl. Phys. Lett.* **2010**, *97*, 033309.
(22) Saba, M. I.; Melis, C.; Colombo, L.; Malloci, G.; Mattoni, A. *J. Phys. Chem. C* **2011**, *115*, 9651−9655.
(23) Dag, S.; Wang, L. W. *Nano Lett.* **2008**, *8*, 4185−4190.
(24) Sai, N.; Leung, K.; Chelikowsky, J. R. *Phys. Rev. B* **2011**, *83*, 121309(R).
(25) Duncan, W. R.; Stier, W. M.; Prezhdo, O. V. *J. Am. Chem. Soc.* **2005**, *127*, 7941−7951.
(26) Duncan, W. R.; Craig, C. F.; Prezhdo, O. V. *J. Am. Chem. Soc.* **2007**, *129*, 8528−8543.
(27) Li, Z.; Zhang, X.; Lu, G. *J. Phys. Chem. B* **2010**, *114*, 17077−17083.
(28) Tully, J. C. *J. Chem. Phys.* **1990**, *93*, 1061−1071.
(29) Drukker, K. *J. Comput. Phys.* **1999**, *153*, 225−272.
(30) Rego, L. G. C.; Abuabara, S. G.; Batista, V. S. *J. Chem. Phys.* **2005**, *122*, 154709.
(31) Abuabara, S. G.; Rego, L. G. C.; Batista, V. S. *J. Am. Chem. Soc.* **2005**, *127*, 18234−18242.
(32) Li, Z.; Zhang, X.; Lu, G. *Appl. Phys. Lett.* **2011**, *98*, 083303.
(33) Fischer, S. A.; Habenicht, B. F.; Madrid, A. B.; Duncan, W. R.; Prezhdo, O. V. *J. Chem. Phys.* **2011**, *134*, 024102.
(34) Parandekar, P. V.; Tully, J. C. *J. Chem. Phys.* **2005**, *122*, 094102.
(35) Kresse, G.; Hafner, J. *Phys. Rev. B* **1993**, *47*, 558−561.
(36) Kresse, G.; Furthmuller, J. *Phys. Rev. B* **1996**, *54*, 11169−11186.
(37) Perdew, J. P.; Burke, K.; Ernzerhof, M. *Phys. Rev. Lett.* **1996**, *77*, 3865−3868.
(38) Perdew, J. P.; Emzerhof, M.; Burke, K. *J. Chem. Phys.* **1996**, *105*, 9982−9985.
(39) Adamo, C.; Barone, V. *J. Chem. Phys.* **1999**, *110*, 6158−6170.
(40) Kanai, Y.; Grossman, J. C. *Nano Lett.* **2007**, *7*, 1967−1972.
(41) Meyer, B.; Marx, D. *Phys. Rev. B* **2003**, *67*, 035403.
(42) Ozgur, U.; Alivov, Y. I.; Liu, C.; Teke, A.; Reshchikov, M. A.; Dogan, S.; Avrutin, V.; Cho, S. J.; Morkoc, H. *J. Appl. Phys.* **2005**, *98*, 041301.
(43) Woll, C. *Prog. Surf. Sci.* **2007**, *82*, 55−120.
(44) Prosa, T. J.; Winokur, M. J.; Moulton, J.; Smith, P.; Heeger, A. J. *Macromolecules* **1992**, *25*, 4364−4372.
(45) Lap, D. V.; Grebner, D.; Rentsch, S. *J. Phys. Chem. A* **1997**, *101*, 107−112.
(46) Liu, T.; Troisi, A. *J. Phys. Chem. C* **2011**, *115*, 2406−2415.
(47) Ravirajan, P.; Peiro, A. M.; Nazeeruddin, M. K.; Graetzel, M.; Bradley, D. D. C.; Durrant, J. R.; Nelson, J. *J. Phys. Chem. B* **2006**, *110*, 7635−7639.
(48) Lin, Y. Y.; Lee, Y. Y.; Chang, L. W.; Wu, J. J.; Chen, C. W. *Appl. Phys. Lett.* **2009**, *94*, 063308.
(49) Vukmirovic, N.; Wang, L. W. *Appl. Phys. Lett.* **2010**, *97*, 043305.
(50) Serrano, J.; Manjon, F. J.; Romero, A. H.; Ivanov, A.; Cardona, M.; Lauck, R.; Bosak, A.; Krisch, M. *Phys. Rev. B* **2010**, *81*, 174304.